HHS Public Access

Author manuscript

Sci Signal. Author manuscript; available in PMC 2021 November 04.

Published in final edited form as:

Sci Signal. ; 14(681): . doi:10.1126/scisignal.abd7325.

Remodeling of the Homer-Shank interactome may mediate homeostatic plasticity

Whitney E. Heavner[1], **Jonathan D. Lautz**[1], **Haley E. Speed**[1], **Edward P. Gniffke**[1], **Karen B. Immendorf**[1], **John P. Welsh**[1,2,3,4], **Nathan A. Baertsch**[1,2], **Stephen E.P. Smith**[1,2,4,*]

[1]Center for Integrative Brain Research, Seattle Children's Research Institute, Seattle, WA, 98101.

[2]Department of Pediatrics, University of Washington School of Medicine, Seattle, WA, 98195.

[3]University of Washington Autism Center, Seattle, WA, 98195.

[4]Graduate Program in Neuroscience, University of Washington, Seattle, WA, 98195.

Abstract

Neurons maintain stable levels of excitability using homeostatic synaptic scaling, which adjusts the strength of a neuron's postsynaptic inputs to compensate for extended changes in overall activity. Here, we investigated whether prolonged changes in activity affect network-level protein interactions at the synapse. We assessed a glutamatergic synapse protein interaction network (PIN) composed of 380 binary associations among 21 protein members in mouse neurons. Manipulating the activation of cultured mouse cortical neurons induced widespread bidirectional PIN alterations that reflected rapid rearrangements of glutamate receptor associations involving synaptic scaffold remodeling. Sensory deprivation of the barrel cortex in live mice (by whisker trimming) caused specific PIN rearrangements, including changes in the association between the glutamate receptor mGluR5 and the kinase Fyn. These observations are consistent with emerging models of experience-dependent plasticity involving multiple types of homeostatic responses. However, mice lacking *Homer1* or *Shank3B* did not undergo normal PIN rearrangements, suggesting that the proteins encoded by these autism spectrum disorder-linked genes may serve as structural hubs for synaptic homeostasis. Our approach demonstrates how changes in the protein content of synapses during homeostatic plasticity translate into functional PIN alterations that may mediate changes in neuron excitability.

Introduction

Neurons maintain constant relative cell-wide synaptic strength, despite varying network activity, through a non-Hebbian form of neural plasticity called homeostatic synaptic scaling (1). At the molecular level, homeostatic α-amino-3-hydroxy-5-methyl-4-isoxazolepropionic

*Corresponding author. seps@uw.edu.

Author contributions: W.E.H. and S.E.P.S designed the study. W.E.H., H.S., N.A.B., J.L., K.I., and E.G. performed the experiments. W.E.H., H.S., N.A.B., J.L., and S.E.P.S. analyzed the data. W.E.H., H.S., N.A.B., and S.E.P.S. wrote the manuscript.

Competing interests: The authors declare that they have no competing interests.

Data and materials availability: All data needed to evaluate the conclusions in the paper are present in the paper or the Supplementary Materials. The raw QMI data files have been deposited to Dryad, accession ID: https://doi.org/10.5061/dryad.pg4f4qrp5.

acid (AMPA)-ergic scaling adjusts the number of postsynaptic glutamate receptors up or down to compensate for prolonged decreased or increased synaptic activity, without compromising the distributed information content of each synapse (2, 3). It has been suggested that synaptic scaling my cooperate with other homeostatic mechanisms, such as homeostatic intrinsic plasticity (4) and sliding-threshold plasticity (also called the "BCM model") (5), in vivo, which stabilize the activity of a neuron within a set-point range during periods of prolonged sensory deprivation (6, 7) or prolonged activation (8) [reviewed in (9)]. Homeostatic plasticity is thought to be crucial for preventing synaptic saturation, thus allowing for new memory formation, and may be disrupted in several neurological disorders, including Alzheimer's disease (10) and autism spectrum disorder (ASD) (11, 12).

Prior studies have catalogued extensive molecular alterations associated with homeostatic scaling. At the most basic level, upscaling is mediated by insertion of AMPA receptors (AMPARs)—evidence exists for involvement of both AMPAR subunits GluA1 (13) and GluA2 (14)—downstream of activity responsive signaling cascades, such as retinoic acid (13) and tumor necrosis factor α (TNFα) (15) signaling, and alterations to AMPAR interactions with synaptic scaffolds. In addition, widespread changes in protein ubiquitination have been documented during scaling (16), and omics-scale studies have identified global transcriptome (17) and proteome (18) alterations. However, mRNA levels do not predict protein expression in complex systems (19), and protein levels *alone* do not determine physiological outcomes. The interactions between newly synthesized or degraded molecules and the existing protein complexes in the cell determine the physiological effects of altered protein turnover. Here, by quantitatively measuring changes to the macromolecular complexes that control the localization of glutamate receptors at the postsynapse, we begin to bridge the molecular gap between well-characterized protein abundance changes and the electrophysiological responses to prolonged activity perturbation.

Results

We treated cultured cortical neurons for 48 hours with tetrodotoxin (TTX) to induce upscaling, bicuculine (BIC) to induce downscaling, or dimethylsulfoxide (DMSO), a vehicle control, and confirmed upscaling and downscaling altered the surface expression of glutamate ionotropic receptor AMPA type subunit 1 (GluA1) (20) (Fig. 1B), the abundance of several synaptic proteins measured by western blot (16) (fig. S1, A and B), and the relative levels of phosphorylated (p-) ERK1/2 (21) (fig. S1C). Electrophysiological voltage-clamp recordings also confirmed that cultures treated with TTX exhibited an increase in the amplitude and frequency of miniature excitatory postsynaptic currents (mEPSCs), whereas the amplitude and frequency of mEPSCs was reduced in cultures treated with BIC (Fig. 1C), consistent with early reports describing the effects of prolonged activity perturbation in vitro (1, 22).

We next evaluated changes in synaptic protein complexes after 48 hours of upscaling or downscaling using quantitative multiplex immunoprecipitation (QMI) (23–25) (Fig. 1A). We refer to multiprotein complexes detected by QMI as "Proteins in Shared Complexes detected by surface Epitopes" (PiSCES), to highlight the fact that the 380 measured associations

among 21 target proteins (table S1) are not necessarily direct. Network-level differences between TTX, BIC, and DMSO-treated cells were evaluated using hierarchical clustering (Fig. 1D) and principal component analysis (PCA) (Fig. 1E), which demonstrated that there is more similarity within each treatment group than between groups, implying that prolonged increased or decreased activity causes distinct network-level changes in synaptic PINs. Weighted correlation network analysis (CNA) (24, 26) identified one primary module that was positively correlated with TTX and negatively correlated with BIC (marked by turquoise on the figure: Fig. 1F). This module was merged with PiSCES that were deemed significant by adaptive nonparametric analysis with an empirical alpha cutoff (ANC) (24) to identify 26 high-confidence interactions that met the criteria for both independent statistical approaches. These resulting "ANC∩CNA PiSCES" changed bidirectionally between TTX and BIC treatment (Fig. 1G), with the majority of PiSCES increasing in response to TTX and decreasing in response to BIC, although some PiSCES followed the opposite pattern. The direction of change was generally consistent across biological replicates (fig. S1D).

The PIN reflected a rearrangement of PiSCES containing AMPAR or metabotropic glutamate receptors (mGluRs) and members of the membrane-associated guanylate kinase (MAGUK) family, including postsynaptic density protein 95 (PSD95), and synaptic scaffolding proteins, including Homer1. PiSCES containing GluA1 and GluA2 (expressed as GluA1_GluA2) and GluA2_PSD95 increased with TTX and decreased with BIC, while mGluR5_Homer1 and mGluR5_Homer1a exhibited a similar pattern, highlighting an underappreciated role for mGluRs in homeostatic scaling (2). Bidirectional scaffold protein rearrangements were also prevalent. PSD95_SAP97 (synapse-associated protein 97), SAP97_ SAPAP (synapse associated protein 90/PSD-95-associated protein 1), Homer1_SAPAP, Shank1_ SAPAP, and Shank1_PSD95 increased with TTX and decreased with BIC. Conversely, Homer1_panShank and a network of PiSCES involving Shank1, panShank, and CaMKIIa, which phosphorylates SAPAP to promote its turnover during downscaling (27), decreased with TTX and increased with BIC. Collectively, these data demonstrate that, in response to prolonged activity perturbation, neurons adjust synaptic strength through widespread, coordinated, and bidirectional changes in the associations between synaptic scaffold proteins and glutamate receptors.

We next asked whether different PiSCES changed at different timepoints over a 48-hour period of upscaling or downscaling. Unsupervised hierarchical clustering (fig. S1E) identified three major clusters: (i) all TTX samples, (ii) BIC 48-hours, and (iii) BIC 12-hours, BIC 24-hours, and DMSO. Similarly, PCA showed that all three TTX groups separated from DMSO control groups along PC1, and BIC 24- and 48-hour groups separated from DMSO in the opposite direction (fig. S1F). These data suggest that qualitatively uniform PIN alterations became quantitatively stronger over time. CNA supported this hypothesis, yielding one major bidirectional module that was most strongly correlated with TTX or BIC independent of time and showed progressively stronger correlation with each TTX and BIC timepoint (fig. S1G).

At 12 hours, seven "fast and stable" PiSCES were ANC∩CNA-significant for each treatment, all of which were significant in at least one future timepoint (Fig. 1H). For TTX, elevated GluA2_GluA1 and Homer1_mGluR5 reflected a rapid and persistent increase in

AMPAR multimerization and mGluR associations with synaptic scaffolding proteins; the opposite occurred for BIC. By 24 hours, in addition to persistent changes in Homer1_mGluR and AMPAR interactions, ubiquitin-protein ligase E3A (UBE3A)_Shank interactions peaked, mGluR5_mGluR5 increased with TTX/decreased with BIC, and PSD95_PSD95 increased with BIC, reflecting changes in protein turnover and abundance. By 48 hours of BIC treatment, we observed increased association of Fyn kinase, which phosphorylates NMDARs to adjust the threshold for LTP, with NMDAR2A, NMDAR2B, and mGluR5 (28, 29). Conversely, by 48 hours of TTX treatment, Fyn interactions with NMDAR and mGluR5 decreased, while changes to a network of PSD95 and Shank1-containing interactions stabilized. Collectively, treatment of cortical cultures with TTX and BIC induced consistent, bidirectional PiSCES changes that increased in magnitude over 48 hours, beginning with rapid Homer1-containing changes to mGluR5 and AMPAR PINs, evolving to NMDAR-associated changes involving PSD95, UBE3A and FYN.

Extreme sensory deprivation of the eyes or whiskers is known to cause synaptic scaling in some layers of the rodent visual and somatosensory (barrel) cortex, respectively; however, in response to prolonged changes to sensory input, neurons can also engage other types of plasticity, including Hebbian and sliding threshold plasticity (reviewed in (9)). Multiple coordinated types of plasticity within a circuit can therefore overlap in a single deprivation paradigm. To model the effect of prolonged sensory deprivation on PIN alterations in vivo, we unilaterally trimmed the whiskers of adult mice and microdissected barrel cortex after 48 hours (Fig. 2A). To confirm that whisker trimming initiated synaptic plasticity, we recorded miniature excitatory postsynaptic currents (mEPSCs) from layer II/III (L2/3) pyramidal neurons, and found that cells contralateral to the whisker trim exhibited a two-fold increase in mean frequency compared with the ipsilateral (control) hemisphere (Fig. 2B,C) with no significant change in mean mEPSC amplitude (fig. S2A). Cumulative analysis of inter-event intervals revealed a global trend toward decreased time between events onto neurons from the contralateral (trimmed) hemisphere compared with those from the ipsilateral hemisphere (fig. S2B), and the cumulative probability of mEPSC amplitude was skewed, revealing a trend toward smaller events that was not reflected in the mean amplitude (fig. S2C). The difference between mean and cumulative probability of mEPSC amplitude could be a result of variability in L2/3 responses between animals during the first three days of whisker deprivation as previously reported (30), overlapping Hebbian and homeostatic plasticity in L2/3, and/or noise caused by residual afferent activity after whisker deprivation similar to that seen in the visual cortex after lid suture (31). In addition, there was no difference in spine density between ipsilateral and contralateral hemispheres (Fig. 2D). These data are consistent with prior reports showing depression in L2/3 of barrel cortex and increased transmission of L4 onto L2/3 during the first three days of whisker deprivation in adult mice (30). While these measurements were limited to L2/3, our microdissections for QMI encompassed the entire cortex, so PIN changes could reflect simultaneous and heterogenous plasticity processes, including multiplicative downscaling in barrel cortex L5 (30, 32). Given this heterogeneity, we here refer to the network response broadly as “experience dependent plasticity.”

Hierarchical clustering (Fig. 2E) and PCA (fig. S2D) of PiSCES measurements taken from micro-dissected control and whisker-deprived (“trimmed”) barrel cortex showed separation

of control and trimmed sides. Uniform Manifold Approximation and Projection (UMAP) of mean $\log_2$(fold change) values taken from 18 independent experiments (72 replicates) demonstrated that BIC, TTX, and whisker trimming each clustered independently (Fig. 2F). ANC∩CNA identified 22 high-confidence PiSCES that changed in response to whisker trimming (Fig. 2G). These included the AMPAR and mGluR-containing PiSCES GluA2_PSD95 (decreased), mGluR5_Homer (increased), and mGluR5_Homer1a (increased), similar to what we observed during in vitro synaptic scaling. Rearrangements in synaptic scaffold proteins were also apparent, with PSD95-, SAP97-, Shank1- and Homer-containing PiSCES uniformly increasing with trimming. NMDAR-associated plasticity was reflected in increased associations between NMDARs and SynGAP, Shank, and Fyn (28), similar to late-stage in vitro synaptic scaling. However, only 11 of the 22 PiSCES that changed in vivo also changed significantly in vitro (Fig. 2H). Moreover, the direction of the change in vivo was consistent with TTX treatment 6 out of 11 times and consistent with BIC treatment 4 out of 11 times (Fig. 2H). Overall, these data demonstrate that sensory deprivation induced an experience-dependent plasticity PIN response that is distinct from the PIN response to in vitro synaptic scaling.

A summary of PiSCES ranked as having the most significant pairwise differences between TTX and BIC, TTX and whisker trimming, and BIC and whisker trimming (table S2) were categorized by function (Fig. 3). Collectively, these data indicate that prolonged changes in global activity levels induced widespread remodeling of synaptic PINs often involving the scaffolding protein Homer1 (Fig. 3, green). The dominant-negative short isoform of Homer1, Homer1a, is required for downscaling during sleep (33) and was involved in several significant synaptic-scaling-associated PIN alterations. We therefore asked whether Homer1 is required for synaptic PIN rearrangements after whisker trimming. We unilaterally whisker-trimmed *Homer1* knockout (KO) mice (34) and measured PiSCES by QMI. PCA revealed that WT and KO samples, regardless of trimming, separated along PC1 and PC2, while WT trimmed and control samples separated along PC3 (Fig. 4A). KO trimmed and control samples, however, showed no clear separation. ANC∩CNA heatmapping revealed widespread dysregulation of the Homer-Shank-mGluR axis in mutant animals (Fig. 4B, below dashed line), including apparent upregulation of some Homer-containing interactions due to our capture antibody showing some cross-reactivity to Homer2. When only those PiSCES that changed significantly after trimming in WT animals (Fig. 4B, above dashed line) were visualized by heatmap, PIN alterations could be observed only in WT, but not KO, animals (Fig. 4C), demonstrating a failure of plasticity in the absence of Homer1. In addition, many PiSCES that were increased after WT whisker trimming were already increased in the *Homer1* KO barrel cortex without whisker trimming, including Shank1_Fyn and mGluR5_Fyn (Fig. 4D), while other PiSCES that increased after whisker trimming in WT animals, such as Shank1_Homer1a, were absent or otherwise unchanged in KO animals (Fig. 4D). While SynGAP_Fyn and SynGAP_NMDAR1 interactions failed to increase in *Homer1* KOs, SynGAP_SynGAP and SynGAP_PSD95 increased after whisker trimming (Fig. 4D), indicating that the system registered a change in sensory input but the excitatory synaptic PIN did not respond at the level observed in WT animals.

The ASD-associated protein Shank3 interacts directly with Homer1 and is required for homeostatic plasticity in the mouse visual cortex after prolonged monocular deprivation

(35). To determine if the loss of Shank3 produces a similar network-scale disruption during homeostatic plasticity, we unilaterally whisker-trimmed adult *Shank3B* KO mice (36) and measured PiSCES by QMI. PCA showed that WT trimmed and untrimmed samples separated along PC1 and PC2, while KO trimmed and untrimmed samples showed no clear separation and overlapped substantially with the WT trimmed group (Fig. 4E). ANC∩CNA heatmapping showed milder basal network dysregulation in untrimmed *Shank3B* KO animals compared with *Homer1* KO animals (Fig. 4F, below dashed line). When only those PiSCES that changed significantly after trimming in WT animals (Fig. 4F, above dashed line) were visualized by heatmap, WT trimmed and control sides could again be distinguished, but not KO trimmed and control sides (Fig. 4G). Moreover, similar to *Homer1* KO results, several PiSCES that were altered after whisker trimming in the WT barrel cortex were already altered in the *Shank3B* KO barrel cortex without whisker trimming, including SAP97_PSD95 and PSD95_PSD95 (Fig. 4H). We also noticed a relative basal increase in PIKE_Shank3 in KO animals compared with WT animals, which could indicate changes in an association involving residual expression of the short "γ" isoform in the *Shank3B* KO (36). SynGAP_PSD95 increased after trimming regardless of genotype (Fig. 4H), also similar to *Homer1* KOs. Thus, Shank-Homer scaffolding is integral to the ability of the barrel cortex to maintain homeostasis in response to prolonged sensory deprivation, and animals lacking either of these scaffolding proteins show a common lack of PIN rearrangements upon whisker trimming.

Discussion

We have used an emerging proteomic technique—QMI—to establish that prolonged activity manipulation of neurons, in vitro and in vivo, causes widespread changes in a synaptic PIN that links three major classes of glutamate receptors known to adjust synaptic strength in response to changes in activity. Our data demonstrate that a synaptic PIN changes bidirectionally with upscaling and downscaling; however, there were more "late" PiSCES changes associated with upscaling than with downscaling, suggesting that upscaling and downscaling may operate on different timescales. While activity perturbation resulted in many stable bidirectional PiSCES changes after only 12 hours, almost half of the significant changes for upscaling were not observed until 48 hours. It has been suggested that upscaling in vivo, which has been observed to occur over days to weeks in the barrel cortex, is necessarily slow in order to avoid saturation and excitotoxicity (30). Similarly, in the adult mouse visual cortex, L2/3 mEPSCs scale up over two days of dark exposure and scale down to baseline after only two hours of light re-exposure (37, 38). Our data suggest that even in a controlled in vitro system, upscaling may involve a slowly evolving PIN that is not observed, or not observed at the same magnitude, in downscaling.

In vivo changes to the synaptic PIN in response to sensory deprivation exhibited unique features as well as features associated with in vitro upscaling and downscaling, consistent with the emerging model that in vivo homeostatic compensation may involve several types of plasticity, including sliding-threshold metaplasticity, local synaptic scaling, and global synaptic scaling, dependent on age, time point, brain region, cell type, and activity regime (31, 39). Cell type-specific homeostatic responses to whisker deprivation have been documented: while L2/3 pyramidal neurons and L5 intrinsic bursting (IB) cells exhibit

features of downscaling during the first three days of full whisker deprivation, L5 regular spiking (RS) cells exhibit features of both downscaling and Hebbian-like LTD, and L4 neurons show upscaling-like homeostatic recovery from depression as early as 12 hours after full deprivation (30, 32). This increased L4 transmission is perhaps a result of reduced intrinsic excitability of L2/3 inhibitory neurons (40). Though the majority of excitatory cells in the barrel cortex are likely undergoing downscaling during the timeframe tested in the current study, our QMI analysis may have also captured features of upscaling, downscaling, and/or Hebbian-like metaplasticity in vivo. It has been suggested that although experience-dependent homeostatic plasticity persists in adulthood in L2/3 of visual cortex, the multiplicative nature of synaptic scaling does not persist; rather, visual deprivation reduces the synaptic modification threshold along a sliding scale, and increased spontaneous activity potentiates synapses, except in cases of extreme deprivation that abolish activity (31). Along the same lines, our results suggest that there are fundamental differences between synaptic PIN rearrangements during synaptic scaling in vitro and experience-dependent plasticity in vivo that reflect an emerging model of multiple mechanisms coordinating to stabilize networks during prolonged periods of sensory deprivation.

Our finding that mice lacking either of the ASD-linked genes *Homer1* or *Shank3* failed to exhibit homeostatic PIN alterations highlights the prominent role of the Homer-Shank axis and supports the hypothesis that disruptions to PINs that mediate synaptic plasticity may underlie multiple rare genetic forms of ASD (41). Previous work has shown that neurons lacking Homer1a exhibit increased mean amplitude of mEPSCs in vitro and in vivo, which may create a “ceiling effect” that impairs synaptic scaling of AMPARs in vitro (2) and occludes experience-dependent homeostatic plasticity in vivo (42). Evidence from these studies also suggests that altered Homer-mediated mGluR5 signaling may underlie this ceiling effect; *Homer1a* expression reduces the amount of mGluR5 associated with Homer1 during downscaling (2), and mice with point mutations in mGluR5 that reduce its Homer1a binding affinity have impaired downscaling in the visual cortex after light re-exposure (42). Similarly, complete *Shank3* KO mice show reduced Homer1-mGluR5 association in the striatum (43), and *Shank3B* KO mice show higher spontaneous calcium event rates in somatosensory cortex (44) and lack homeostatic compensation during monocular deprivation (35). Our observation that both *Homer1* and *Shank3* KO mice appear to be molecularly “pre-scaled,” or have baseline altered synaptic PINs consistent with sensory deprivation, provides further evidence for a “ceiling effect” that occludes a homeostatic response to changes in network activity. While Homer1 and Shank3 have been implicated in homeostatic compensation in vivo (33, 35, 42), the disruption to scaffold rearrangements during sensory deprivation reported here has not been described previously.

Building on these prior studies, we have identified a synaptic PIN involving the Homer-Shank scaffold that mediates homeostatic scaling in vitro and experience-dependent plasticity in vivo. Collectively, these results support a model whereby an inability to homeostatically compensate for prolonged activity perturbation may be a unifying feature of some ASDs. It will be important for future studies to test the ability of therapeutic interventions to restore homeostatic plasticity in ASD models.

Materials and Methods

Animals:

All animal work was carried out in compliance with The Seattle Children's Research Institute IACUC under approved protocol #00072 and institutional and federal guidelines. CD-1 and *Homer1*^{tm1Mhd} (stock 023312), and *Shank3*^{tm2Gfng} (stock 017688) mice were originally obtained from The Jackson Laboratory (Bar Harbor, ME).

Genotyping:

0.2 μL of crude DNA extract (KAPA Biosystems) from ear punch tissue was used for genotyping the Homer1^{tm1Mhd} allele with the following primers: 5'-CAA TGC ATG CAA TTC CTG AG-3', 5'-CGA GAA ACT TAC ATA TAT CCG CAA A-3', and 5'-GAA CTT CGC GCT ATA ACT TCG-3' (The Jackson Laboratory), or the Shank3B^{-} allele with the following primers: 5'-GAG ACT GAT CAG CGC AGT TG-3', 5'-TGA CAT AAT CGC TGG CAA AG-3', 5'-GCT ATA CGA AGT TAT GTC GAC TAG G-3' using standard PCR protocols.

Whisker trimming:

Mystacial whiskers on one side of an adult mouse (7 to 9 weeks of age) were removed with an electric trimmer while the mouse was under very brief isoflurane anesthesia. Lysates were prepared, as described below, 48 hours after trimming.

Cortical neuron culture, drug treatment, and surface labeling:

Primary cultures of cortical neurons were prepared as previously described (23). Briefly, whole cortex from P0-P1mouse neonates was dissociated using papain (Worthington) and plated at a density of 1.0×10^6 cells/well onto 6-well plates treated with poly-D-lysine. Cells were cultured in Neurobasal medium supplemented with 2% B27 and 0.5mM GlutaMax (ThermoFisher) and kept at 37°C, 5% CO_2 for 18–21 days. After 3–5 DIV, 5-fluoro-2'-deoxyuridine was added to a final concentration of 5 μM to inhibit glial proliferation. For in vitro homeostatic scaling experiments, TTX (2μM) or BIC (40μM) (Tocris) was added directly to the culture medium, and cells were cultured as normal, then lysed after 12, 24, or 48 hours. DMSO (0.4%) served as a vehicle control.

For surface labeling of GluA1, cortical cells were dissociated and cultured as above, with the following exceptions: cells were plated at a density of 0.1×10^6 cells/well on glass coverslips treated with poly-D-lysine in 24-well plates. A mouse antibody to the N-terminus of GluA1 conjugated with Alexa Fluor 488 (G-12, Santa Cruz Biotechnology) was added to primary neuron cultures (18–21 DIV) to a final concentration of 4μg/mL (1:50 dilution), and cells were kept at 37°C, 5% CO_2 for 20 minutes. Culture medium was then removed, and cells were washed once with 1X PBS and fixed with pre-warmed 4% PFA/4% sucrose in 1X PBS at room temperature for 10 minutes shielded from light. After fixation, cells were washed twice with 1X PBS and mounted on glass slides using ProLong Antifade Mountant with DAPI (Invitrogen). Cells were imaged on a Zeiss LSM 710 at 100X. Mean gray values of 8-bit images were calculated in the green channel after thresholding using default settings in

ImageJ. Nine cells from at least 3 independent experiments were included in the final analysis. A paired two-tailed Student's t-Test was used to determine significance.

Lysate preparation:

After treatment of cultured cells, cell culture medium was removed and cells were scraped in cold lysis buffer (150mM NaCl, 50mM Tris pH 7.5, 1% NP-40, 10mM Sodium Fluoride, 2mM sodium orthovanadate, protease inhibitor cocktail (Sigma) and phosphatase inhibitor cocktail (Sigma)), transferred to a centrifuge tube, incubated on ice for 15 minutes, and centrifuged at high seed for 15 minutes to remove nuclei and debris. The protein concentration of the supernatant was determined using a Bradford assay (Pierce).

Lysates from cortical slices were prepared as above with the following exceptions: Adult mice were anesthetized with isoflurane and perfused through the heart with ice cold 1X PBS. Brains were immediately removed, placed into cold PBS, and sliced in cold PBS using a VT1200s vibrating microtome (Leica). Five 500μm slices through the somatosensory (barrel) cortex were divided into ipsilateral and contralateral hemispheres, the barrel cortex microdissected away from the rest of the slice and kept briefly in ice cold PBS. All microdissected slices from one hemisphere were then combined, transferred to lysis buffer, and mechanically dissociated using a PYREX tissue grinder.

Western Blotting:

For Western blots, proteins (20 μg per lane) were separated by SDS-PAGE and transferred to a PVDF membrane (Millipore). Membranes were blocked in 4% milk in TBST (0.05M Tris pH7.2, 0.15M NaCl, 0.1% Tween20) for 1 hour at room temperature and incubated with primary antibodies overnight at 4°C or for 1 hour at room temperature. Primary antibodies and dilutions used for western blots were Fyn (clone 59, BioLegend, 1:1000), GluA1 (1504, Millipore, 0.001 mg/ml), Homer1 (AT1F3, LSBio, 1:1000), mGluR5 (5675, Millipore, 1:2000), PSD95 (K28/43, BioLegend, 1:500), beta-Actin (GTX109639, GeneTex, 1:10,000), p-ERK T202/Y204 (4370, Cell Signaling Technologies, 1:1000), and total ERK (9102, Cell Signaling Technologies, 1:1000). Primary antibodies were detected using species-specific HRP-conjugated secondary antibodies. Blots were developed using Femto Maximum Sensitivity Substrate (Pierce) and imaged using a ProteinSimple imaging system (San Jose, CA).

Quantitative multiplex immunoprecipitation:

QMI was performed as described previously (23, 24) using previously validated antibodies (23). Briefly, a master mix containing equal numbers of each antibody-coupled Luminex bead was prepared and distributed to lysates containing equal amounts of protein and incubated overnight on a rotator at 4°C. The next day, each sample was washed twice in cold Fly-P buffer (50mM tris pH7.4, 100mM NaCl, 1% bovine serum albumin, and 0.02% sodium azide) and distributed into twice as many wells of a 96-well plate as there were probe antibodies (for technical duplicates). Biotinylated detection (probe) antibodies were added to the appropriate wells and incubated at 4°C with gentle agitation for 1 hour. The resulting bead-probe complexes were washed 3 times with Fly-P buffer, incubated for 30 minutes with streptavidin-PE on ice, washed another 3 times, resuspended in 125μl ice cold

Fly-P buffer, and processed for fluorescence using a customized refrigerated Bio-Plex 200 (24). Antibody clone names, catalog numbers, and lot numbers are the same as in (23).

Our analysis was then designed to achieved inter-experimental consistency. QMI attempts to measure unstable protein-protein interactions within noisy and stochastic intracellular environments and thus faces reproducibility challenges similar to mass spectrometry (45, 46). While noise is inherent to all signal transduction experiments, we are uniquely able to bioinformatically sort signal from noise using CNA modules. We previously established that QMI consistently identifies significant PiSCES changes in N-of-4 experiments (23, 24). However, we noticed that while sample-to-sample consistency was very high for samples that were run simultaneously (meaning, cells grown and lysed in parallel and run on the same assay plate, as in fig. S3A), samples that were prepared separately showed less consistent overlap (as in fig. S3B). We therefore performed three independent replicates of N-of-4 or N-of-5 experiments and combined the data into a larger N-of-13 set for CNA. (ANC, which was designed for only N-of-4 to 8 samples, becomes overly stringent at identifying true positives over an N-of-4 (24)). In the three independent experiments, there was only moderate agreement in PiSCES identified by ANC and CNA (fig. S3B). However, when any significant PiSCES that was identified in any one of the three experiments was visualized by heatmap (Fig. 1G) and/or bar graph (fig. S3C), it became apparent that PiSCES changes trended in the same direction for all experiments. In other words, our analysis stringently identified high-confidence PiSCES in individual experiments that constituted a subset of the total PiSCES that actually changed. When multiple experiments were compared, each experiment identified a different subset of the total PiSCES. This is consistent with reproducibility rates reported for mass spectrometry, which faces a similar problem of only identifying a subset of all true positives in any one experiment (45, 46).

ANC:

High-confidence, statistically significant differences in bead distributions between two conditions for individual PiSCES, after correcting for multiple comparisons, were identified using ANC as described in (24). Any PiSCES that was found to be significant by any ANC comparison was considered a “hit”.

CNA:

Modules of PiSCES that co-varied with experimental conditions were identified using CNA as described in (23, 24). Briefly, bead distributions used in ANC were collapsed into a single MFI value for every PiSCES and averaged across technical replicates for input into the WGCNA package for R (26). PiSCES with MFI < 100 were removed, and batch effects were corrected using COMBAT (47). Power values giving the approximation of scale-free topology were determined using soft thresholding with a power adjacency function. The minimum module size was always set to between 10 and 12, and modules whose eigenvectors significantly correlated with an experimental trait (P<0.05) were considered “of interest.” PiSCES belonging to a module of interest and whose probability of membership in that module was >0.7 (P<0.05) were considered significant. PiSCES that were significant by both ANC and CNA for a given experimental condition were considered significantly altered in that condition.

Hierarchical clustering and PCA:

Post-COMBAT, $\log_2$ transformed MFI values were clustered using the hclust function in R with a correlation distance matrix and average clustering method. Approximately unbiased (AU) *P*-values were determined using the pvclust package in R (48). PCA was performed using the prcomp function in R.

UMAP:

Uniform manifold approximation and projection (UMAP) (49) was performed using the umap function in R, mean $\log_2$(fold change) over control of each PiSCES that was significant in any condition for each set of experiments (4 biological replicates per set, 18 sets total) as input, and default settings with nearest neighbors set to 10. The most significantly different PiSCES between UMAP groups were determined by Wilcoxon rank-sum pairwise comparisons of sets grouped by UMAP cluster in R. Heatmaps were generated using Heatmap.2 in R.

Patch clamp recording from cortical cultures:

Cortical neuron cultures were prepared as described above and exposed to either TTX (2 μM), BIC (40 μM) or DMSO (0.4%) for 48 hours. Voltage clamp recordings were performed with the investigator blinded to treatment group. Neuronal cultures were placed in a custom recording chamber containing room temperature artificial cerebrospinal fluid (aCSF; in mM: 118 NaCl, 3.0 KCl, 25 NaHCO3, 1 NaH2PO4, 1.0 MgCl2, 1.5 CaCl2, 10 D-glucose, 20 Sucrose) with an osmolarity of 305–312mOSM and a pH of 7.40. 2μM TTX was also included in the aCSF to prevent action potential evoked presynaptic release. Recordings were performed with electrodes pulled from borosilicate glass (4–8 MΩ tip resistance) using a P-97 Flaming/Brown micropipette puller (Sutter Instrument Co., Novato, CA) and filled with low Cl− internal solution containing (in mM): 140 potassium gluconate, 1 CaCl2, 10 EGTA, 2 MgCl2, 4 Na2ATP, and 10 Hepes (pH 7.2). Under visual control using video-enhanced Dodt-IR optics (Zeiss Axio Examiner.A1 microscope with a 40X water-immersion objective), a >1 GΩ seal was established and maintained prior to entering whole-cell configuration. Only cells with resting Vm < −55 mV were included in the analysis. Intracellular currents were recorded with neurons voltage-clamped at −60 mV. Signals were acquired and digitized at 10 KHz with an Axopatch 1D amplifier and pClamp10.4 (Molecular Devices, Sunnyvale, CA). ~5 min of data was recorded and analyzed from each neuron. mEPSCs amplitudes and interevent intervals were analyzed *post hoc* in Clampfit 11.1 using the template search event detection function. Statistics and data visualization were done using GraphPad Prism 8 software. Each cell was treated as a replicate, and the cumulative probability curves for each cell were averaged in 2pA bins to create a curve with means ± SEM. This method allows different numbers of datapoints (meaning events) to be used from each cell.

Acute slice preparation and recording:

Adult male mice (7–9 weeks old) were anesthetized with isoflurane inhalation anesthetic and perfused through the heart with ice cold standard artificial cerebral spinal fluid (ACSF). Brains were rapidly removed and placed into ice-cold cutting aCSF. 300 μm thalamocortical

slices were cut on a VT1000s vibrating microtome (Leica) and were gently warmed to 35^{O}C for 15–20 minutes then allowed to cool to room temperature prior to recording. All recordings were performed at 32.5 ± 1^{O}C. Barrel cortex LII/III pyramidal neurons were visually identified under DIC optics (Nikon) and confirmed by their electrophysiological profile and *posthoc* morphological reconstruction. Recordings were sampled at 10 KHz with a Multiclamp 700B amplifier Digidata 1400 digitizer (Molecular Devices) and were rejected if $I_{Holding}$ exceeded ± 100 pA from −70 mV in voltage camp or if Vm changed more than 15% in current clamp. Only cells with > 1 GΩ seal and Vm ≤ −55 mV were included in analysis. Junction potential was 13 mV (compensated).

Histology:

Neurobiotin was allowed to passively diffuse throughout the dendritic tree for the duration of each recording (>10 min). The recording pipette was carefully withdrawn and the membrane allowed to re-seal before separation with a tap to the headstage. The slice was immediately transferred to 4% paraformaldehyde for > 1 hour and kept up to 2 weeks at 4^{O}C before processing with streptavidin. PFA was removed with four 15-min washes in 1X PBS and followed with a 2-hour block in 1X PBS + 0.5% Triton X-100 and 10% goat serum. 1% Alexa 488-streptavidin conjugate was added to fresh blocking solution for 1 to 2 hours then washed 4X for 15 min each in 1X PBS. Slices were mounted with Vectashield anti-fade mounting medium with DAPI (Vector Labs) and visualized on a LSM 710 confocal microscope (Zeiss) with 20X, 40X, and 63X objectives. Spines were counted by an observer blind to hemisphere over a 15–50 μm continuous section of dendrites located 100–150 μm from the cell body.

Solutions and drugs:

Standard aCSF was comprised of (in mM) NaCl 128, KCl 3, NaH_2PO_4 1.25, $NaHCO_3$ 26, glucose 10, $CaCl_2$ 2, and $MgSO_4$ 2, at pH 7.35–7.4 and 305–315 mOsm. Cutting ACSF was comprised of (in mM) sucrose 75, NaCl 87, KCl 3, NaH_2PO_4 1.25, $NaHCO_3$ 26, glucose 20, $CaCl_2$ 0.5, and $MgSO_4$ 7, at pH 7.35–7.4 and 305–315 mOsm. The internal recording solution was (in mM) $KmeSO_4$, KCl 7, EGTA 0.1, Na_2ATP 2, MgATP 2, Na_2GTP 0.3, phosphocreatine 5, and 0.2% neurobiotin, at 7.4 pH, 285–295 mOsm. Bath-applied drugs were tetrodotoxin at 1 μM and picrotoxin at 25 μM.

Analysis and statistics:

Raw traces were acquired, offline filtered to 1 KHz, and analyzed with the pClamp software suite (v. 10.7, Molecular Devices). Neuron reconstructions were performed using ShuTu dendrite tracing software (http://personal.psu.edu/dzj2/ShuTu/) and the Sholl Analysis plug-in for FIJI/ImageJ (50). Statistics and plotting were performed with OriginLab Pro 2017.

Supplementary Material

Refer to Web version on PubMed Central for supplementary material.

Acknowledgments:

The authors would like to thank members of the Smith laboratory, especially Emily Brown and Gabriel McHugh, and members of the Center for Integrative Brain Research for helpful discussions.

Funding:

This work was supported by The National Institute of Mental Health, grants MH102244 and MH113545 (SEPS) and NS31224 (JPW).

References and Notes

1. Turrigiano GG, Leslie KR, Desai NS, Rutherford LC, Nelson SB, Activity-dependent scaling of quantal amplitude in neocortical neurons. Nature 391, 892–896 (1998). [PubMed: 9495341]
2. Hu J-H, Park JM, Park S, Xiao B, Dehoff MH, Kim S, Hayashi T, Schwarz MK, Huganir RL, Seeburg PH, Linden DJ, Worley PF, Homeostatic Scaling Requires Group I mGluR Activation Mediated by Homer1a. Neuron 68, 1128–1142 (2010). [PubMed: 21172614]
3. O'Brien RJ, Kamboj S, Ehlers MD, Rosen KR, Fischbach GD, Huganir RL, Activity-dependent modulation of synaptic AMPA receptor accumulation. Neuron 21, 1067–1078 (1998). [PubMed: 9856462]
4. Desai NS, Rutherford LC, Turrigiano GG, Plasticity in the intrinsic excitability of cortical pyramidal neurons. Nat. Neurosci 2, 515–520 (1999). [PubMed: 10448215]
5. Bienenstock EL, Cooper LN, Munro PW, Theory for the development of neuron selectivity: orientation specificity and binocular interaction in visual cortex. J. Neurosci 2, 32–48 (1982). [PubMed: 7054394]
6. Hengen KB, Lambo ME, Van Hooser SD, Katz DB, Turrigiano GG, Firing rate homeostasis in visual cortex of freely behaving rodents. Neuron 80, 335–342 (2013). [PubMed: 24139038]
7. Hengen KB, Torrado Pacheco A, McGregor JN, Van Hooser SD, Turrigiano GG, Neuronal Firing Rate Homeostasis Is Inhibited by Sleep and Promoted by Wake. Cell 165, 180–191 (2016). [PubMed: 26997481]
8. Goold CP, Nicoll RA, Single-cell optogenetic excitation drives homeostatic synaptic depression. Neuron 68, 512–528 (2010). [PubMed: 21040851]
9. Lee H-K, Kirkwood A, Mechanisms of Homeostatic Synaptic Plasticity in vivo. Front Cell Neurosci 13 (2019), doi:10.3389/fncel.2019.00520.
10. Styr B, Slutsky I, Imbalance between firing homeostasis and synaptic plasticity drives early-phase Alzheimer's disease. Nature Neuroscience 21, 463–473 (2018). [PubMed: 29403035]
11. Antoine MW, Langberg T, Schnepel P, Feldman DE, Increased Excitation-Inhibition Ratio Stabilizes Synapse and Circuit Excitability in Four Autism Mouse Models. Neuron 101, 648–661.e4 (2019). [PubMed: 30679017]
12. Bülow P, Murphy TJ, Bassell GJ, Wenner P, Homeostatic Intrinsic Plasticity Is Functionally Altered in Fmr1 KO Cortical Neurons. Cell Rep 26, 1378–1388.e3 (2019). [PubMed: 30726724]
13. Aoto J, Nam CI, Poon MM, Ting P, Chen L, Synaptic signaling by all-trans retinoic acid in homeostatic synaptic plasticity. Neuron 60, 308–320 (2008). [PubMed: 18957222]
14. Gainey MA, Hurvitz-Wolff JR, Lambo ME, Turrigiano GG, Synaptic Scaling Requires the GluR2 Subunit of the AMPA Receptor. J Neurosci 29, 6479–6489 (2009). [PubMed: 19458219]
15. Stellwagen D, Malenka RC, Synaptic scaling mediated by glial TNF-α. Nature 440, 1054–1059 (2006). [PubMed: 16547515]
16. Ehlers MD, Activity level controls postsynaptic composition and signaling via the ubiquitin-proteasome system. Nat. Neurosci 6, 231–242 (2003). [PubMed: 12577062]
17. Schaukowitch K, Reese AL, Kim S-K, Kilaru G, Joo J-Y, Kavalali ET, Kim T-K, An Intrinsic Transcriptional Program Underlying Synaptic Scaling during Activity Suppression. Cell Rep 18, 1512–1526 (2017). [PubMed: 28178527]

18. Schanzenbächer CT, Sambandan S, Langer JD, Schuman EM, Nascent Proteome Remodeling following Homeostatic Scaling at Hippocampal Synapses. Neuron 92, 358–371 (2016). [PubMed: 27764671]
19. Jovanovic M, Rooney MS, Mertins P, Przybylski D, Chevrier N, Satija R, Rodriguez EH, Fields AP, Schwartz S, Raychowdhury R, Mumbach MR, Eisenhaure T, Rabani M, Gennert D, Lu D, Delorey T, Weissman JS, Carr SA, Hacohen N, Regev A, Immunogenetics. Dynamic profiling of the protein life cycle in response to pathogens. Science 347, 1259038–1259038 (2015). [PubMed: 25745177]
20. Diering GH, Gustina AS, Huganir RL, PKA-GluA1 Coupling via AKAP5 Controls AMPA Receptor Phosphorylation and Cell-Surface Targeting during Bidirectional Homeostatic Plasticity. Neuron 84, 790–805 (2014). [PubMed: 25451194]
21. Bateup HS, Denefrio CL, Johnson CA, Saulnier JL, Sabatini BL, Temporal dynamics of a homeostatic pathway controlling neural network activity. Front. Mol. Neurosci 6 (2013), doi:10.3389/fnmol.2013.00028.
22. Rutherford LC, DeWan A, Lauer HM, Turrigiano GG, Brain-Derived Neurotrophic Factor Mediates the Activity-Dependent Regulation of Inhibition in Neocortical Cultures. J. Neurosci 17, 4527–4535 (1997). [PubMed: 9169513]
23. Lautz JD, Brown EA, Williams VanSchoiack AA, Smith SEP, Synaptic activity induces input-specific rearrangements in a targeted synaptic protein interaction network. J. Neurochem 146, 540–559 (2018). [PubMed: 29804286]
24. Smith SEP, Neier SC, Reed BK, Davis TR, Sinnwell JP, Eckel-Passow JE, Sciallis GF, Wieland CN, Torgerson RR, Gil D, Neuhauser C, Schrum AG, Multiplex matrix network analysis of protein complexes in the human TCR signalosome. Sci Signal 9, rs7 (2016). [PubMed: 27485017]
25. Lautz JD, Gniffke EP, Brown EA, Immendorf KB, Mendel RD, Smith SEP, Activity-dependent changes in synaptic protein complex composition are consistent in different detergents despite differential solubility. Sci Rep 9, 10890 (2019). [PubMed: 31350430]
26. Langfelder P, Horvath S, WGCNA: an R package for weighted correlation network analysis. BMC Bioinformatics 9, 559 (2008). [PubMed: 19114008]
27. Shin SM, Zhang N, Hansen J, Gerges NZ, Pak DTS, Sheng M, Lee SH, GKAP/SAPAP orchestrates activity-dependent postsynaptic protein remodeling and homeostatic scaling. Nat Neurosci 15, 1655–1666 (2012). [PubMed: 23143515]
28. Lu YF, Kojima N, Tomizawa K, Moriwaki A, Matsushita M, Obata K, Matsui H, Enhanced synaptic transmission and reduced threshold for LTP induction in fyn-transgenic mice. Eur. J. Neurosci 11, 75–82 (1999). [PubMed: 9987012]
29. Trepanier CH, Jackson MF, MacDonald JF, Regulation of NMDA receptors by the tyrosine kinase Fyn. The FEBS Journal 279, 12–19 (2012). [PubMed: 21985328]
30. Glazewski S, Greenhill S, Fox K, Time-course and mechanisms of homeostatic plasticity in layers 2/3 and 5 of the barrel cortex. Philos. Trans. R. Soc. Lond., B, Biol. Sci 372 (2017), doi:10.1098/rstb.2016.0150.
31. Bridi MCD, de Pasquale R, Lantz CL, Gu Y, Borrell A, Choi S-Y, He K, Tran T, Hong SZ, Dykman A, Lee H-K, Quinlan EM, Kirkwood A, Two distinct mechanisms for experience-dependent homeostasis. Nat. Neurosci 21, 843–850 (2018). [PubMed: 29760525]
32. Greenhill SD, Ranson A, Fox K, Hebbian and Homeostatic Plasticity Mechanisms in Regular Spiking and Intrinsic Bursting Cells of Cortical Layer 5. Neuron 88, 539–552 (2015). [PubMed: 26481037]
33. Diering GH, Nirujogi RS, Roth RH, Worley PF, Pandey A, Huganir RL, Homer1a drives homeostatic scaling-down of excitatory synapses during sleep. Science 355, 511–515 (2017). [PubMed: 28154077]
34. Yuan JP, Kiselyov K, Shin DM, Chen J, Shcheynikov N, Kang SH, Dehoff MH, Schwarz MK, Seeburg PH, Muallem S, Worley PF, Homer binds TRPC family channels and is required for gating of TRPC1 by IP3 receptors. Cell 114, 777–789 (2003). [PubMed: 14505576]
35. Tatavarty V, Torrado Pacheco A, Groves Kuhnle C, Lin H, Koundinya P, Miska NJ, Hengen KB, Wagner FF, Van Hooser SD, Turrigiano GG, Autism-Associated Shank3 Is Essential for Homeostatic Compensation in Rodent V1. Neuron 106, 769–777.e4 (2020). [PubMed: 32199104]

36. Peça J, Feliciano C, Ting JT, Wang W, Wells MF, Venkatraman TN, Lascola CD, Fu Z, Feng G, Shank3 mutant mice display autistic-like behaviours and striatal dysfunction. Nature 472, 437–442 (2011). [PubMed: 21423165]
37. Goel A, Lee H-K, Persistence of Experience-Induced Homeostatic Synaptic Plasticity through Adulthood in Superficial Layers of Mouse Visual Cortex. J. Neurosci 27, 6692–6700 (2007). [PubMed: 17581956]
38. Gao M, Sossa K, Song L, Errington L, Cummings L, Hwang H, Kuhl D, Worley P, Lee H-K, A Specific Requirement of Arc/Arg3.1 for Visual Experience-Induced Homeostatic Synaptic Plasticity in Mouse Primary Visual Cortex. J. Neurosci 30, 7168–7178 (2010). [PubMed: 20505084]
39. Tara Keck, Taro Toyoizumi, Lu Chen, Brent Doiron, Feldman Daniel E., Fox Kevin, Gerstner Wulfram, Haydon Philip G., Hübener Mark, Lee Hey-Kyoung, Lisman John E., Rose Tobias, Sengpiel Frank, Stellwagen David, Stryker Michael P., Turrigiano Gina G., van Rossum Mark C., Integrating Hebbian and homeostatic plasticity: the current state of the field and future research directions. Philosophical Transactions of the Royal Society B: Biological Sciences 372, 20160158 (2017).
40. Gainey MA, Aman JW, Feldman DE, Rapid Disinhibition by Adjustment of PV Intrinsic Excitability during Whisker Map Plasticity in Mouse S1. J. Neurosci 38, 4749–4761 (2018). [PubMed: 29678876]
41. Heavner WE, Smith SEP, Resolving the Synaptic versus Developmental Dichotomy of Autism Risk Genes. Trends in Neurosciences 43, 227–241 (2020). [PubMed: 32209454]
42. Chokshi V, Gao M, Grier BD, Owens A, Wang H, Worley PF, Lee H-K, Input-Specific Metaplasticity in the Visual Cortex Requires Homer1a-Mediated mGluR5 Signaling. Neuron (2019), doi:10.1016/j.neuron.2019.08.017.
43. Wang X, Bey AL, Katz BM, Badea A, Kim N, David LK, Duffney LJ, Kumar S, Mague SD, Hulbert SW, Dutta N, Hayrapetyan V, Yu C, Gaidis E, Zhao S, Ding J-D, Xu Q, Chung L, Rodriguiz RM, Wang F, Weinberg RJ, Wetsel WC, Dzirasa K, Yin H, Jiang Y-H, Altered mGluR5-Homer scaffolds and corticostriatal connectivity in a Shank3 complete knockout model of autism. Nat Commun 7, 11459 (2016). [PubMed: 27161151]
44. Chen Q, Deister CA, Gao X, Guo B, Lynn-Jones T, Chen N, Wells MF, Liu R, Goard MJ, Dimidschstein J, Feng S, Shi Y, Liao W, Lu Z, Fishell G, Moore CI, Feng G, Dysfunction of cortical GABAergic neurons leads to sensory hyper-reactivity in a Shank3 mouse model of ASD. Nat. Neurosci 23, 520–532 (2020). [PubMed: 32123378]
45. Tabb DL, Vega-Montoto L, Rudnick PA, Variyath AM, Ham A-JL, Bunk DM, Kilpatrick LE, Billheimer DD, Blackman RK, Cardasis HL, Carr SA, Clauser KR, Jaffe JD, Kowalski KA, Neubert TA, Regnier FE, Schilling B, Tegeler TJ, Wang M, Wang P, Whiteaker JR, Zimmerman LJ, Fisher SJ, Gibson BW, Kinsinger CR, Mesri M, Rodriguez H, Stein SE, Tempst P, Paulovich AG, Liebler DC, Spiegelman C, Repeatability and Reproducibility in Proteomic Identifications by Liquid Chromatography—Tandem Mass Spectrometry. J Proteome Res 9, 761 (2010). [PubMed: 19921851]
46. Gonzalez-Lozano MA, Koopmans F, Sullivan PF, Protze J, Krause G, Verhage M, Li KW, Liu F, Smit AB, Stitching the synapse: Cross-linking mass spectrometry into resolving synaptic protein interactions. Science Advances 6, eaax5783 (2020). [PubMed: 32128395]
47. Johnson WE, Li C, Rabinovic A, Adjusting batch effects in microarray expression data using empirical Bayes methods. Biostatistics 8, 118–127 (2007). [PubMed: 16632515]
48. Suzuki R, Shimodaira H, Pvclust: an R package for assessing the uncertainty in hierarchical clustering. Bioinformatics 22, 1540–1542 (2006). [PubMed: 16595560]
49. Becht E, McInnes L, Healy J, Dutertre C-A, Kwok IWH, Ng LG, Ginhoux F, Newell EW, Dimensionality reduction for visualizing single-cell data using UMAP. Nat. Biotechnol (2018), doi:10.1038/nbt.4314.
50. Ferreira TA, Blackman AV, Oyrer J, Jayabal S, Chung AJ, Watt AJ, Sjöström PJ, van Meyel DJ, Neuronal morphometry directly from bitmap images. Nature Methods 11, 982–984 (2014). [PubMed: 25264773]

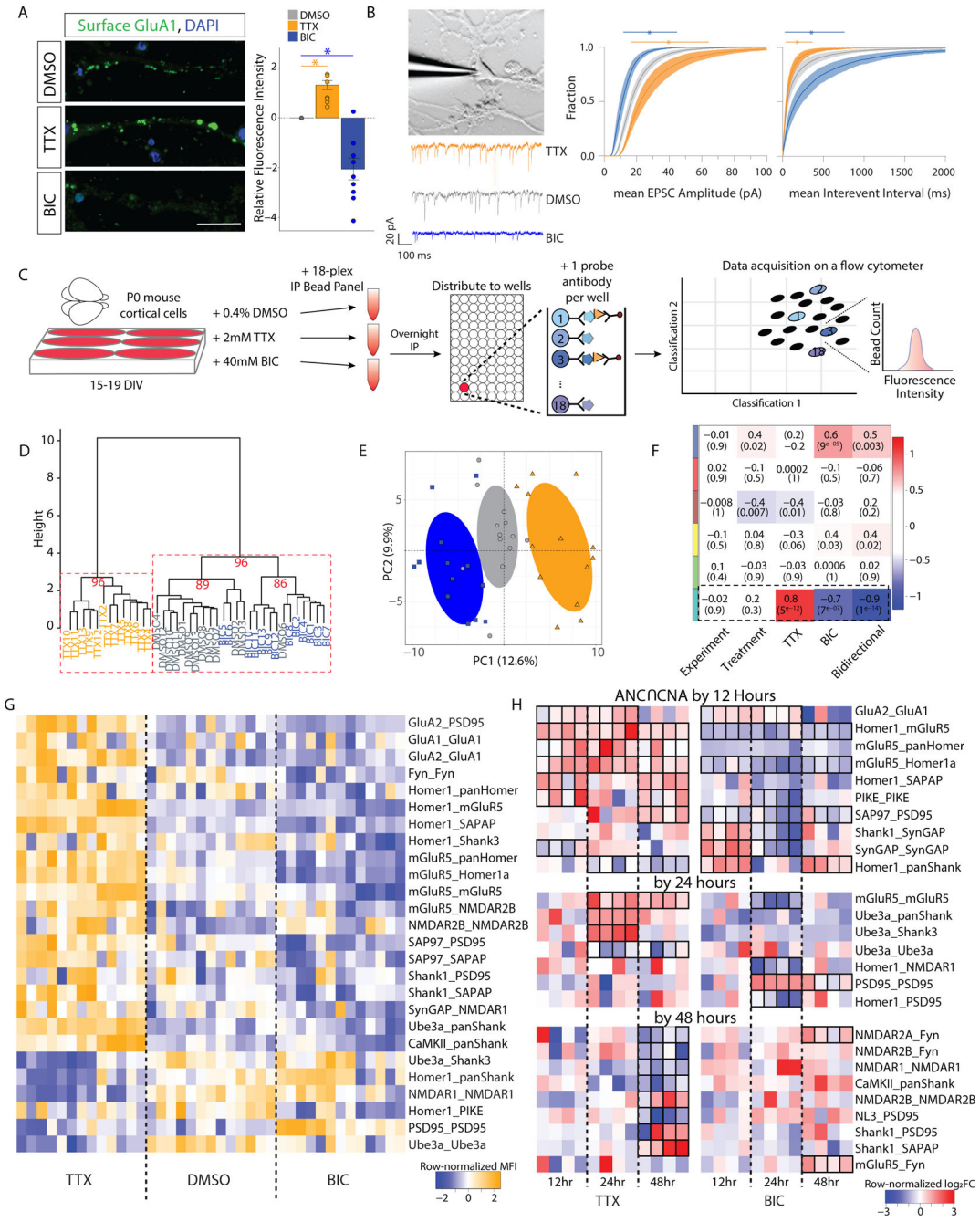

Fig. 1. Prolonged increased or decreased activity of cultured cortical neurons causes network-level changes to multiprotein complexes.

(A) Surface GluA1 (green) and DAPI (nuclei, blue) in cortical neurons treated with DMSO (control), TTX, or BIC. Mean fluorescence intensity of GluA1 relative to control is shown in the scatter plot to the right. Data are from N=9 cells from 3 biological replicates. * $P<0.05$ by Student's t-Test. Scale bar=20μm. **(B)** Representative image of a recorded excitatory neuron and 1s raw traces from TTX-, BIC-, and DMSO-treated cells. Cumulative histograms of mean EPSC amplitude and event frequency from N=8 TTX cells, 15 DMSO cells, and 12 BIC cells from a minimum of 6 cultures. * $P<0.05$ by two-way ANOVA. **(C)** Experimental

design of a QMI experiment illustrating treatment of cultured mouse cortical neurons, multiplexed co-IP, and data acquisition. IP, immunoprecipitation. **(D and E)** Hierarchical clustering (D; AU *P*-values shown in red) and principal component analysis (PCA) (E) of 39 samples representing 3 treatment conditions, each of 13 biological replicates, assessed at 48 hours of treatment. **(F)** Module-trait relationship heatmap showing the correlation (top number) and *P*-value calculated by CNA for each module-trait pair. **(G)** Heatmap of row-normalized MFIs of all Proteins in Shared Complexes (PiSCES) significant by two of two independent statistical tests -- adaptive non-parametric adjusted for multiple comparisons and correlation network analysis (ANC∩CNA). Each column represents an independent replicate; the Nth column of each condition (meaning the first column of each treatment type) was run on the same assay plate. **(H)** Row-normalized heatmaps of the mean $\log_2$(fold change) for ANC∩CNA PiSCES at each of three time points (at 12, 24 and 48 hours). Data are from N=4 biological replicates per time point per condition. Thick outlines indicate sets for which the PiSCES measurement was significantly different from the DMSO condition data by ANC∩CNA. PiSCES are arranged into groups according to the earliest time point at which they became significant.

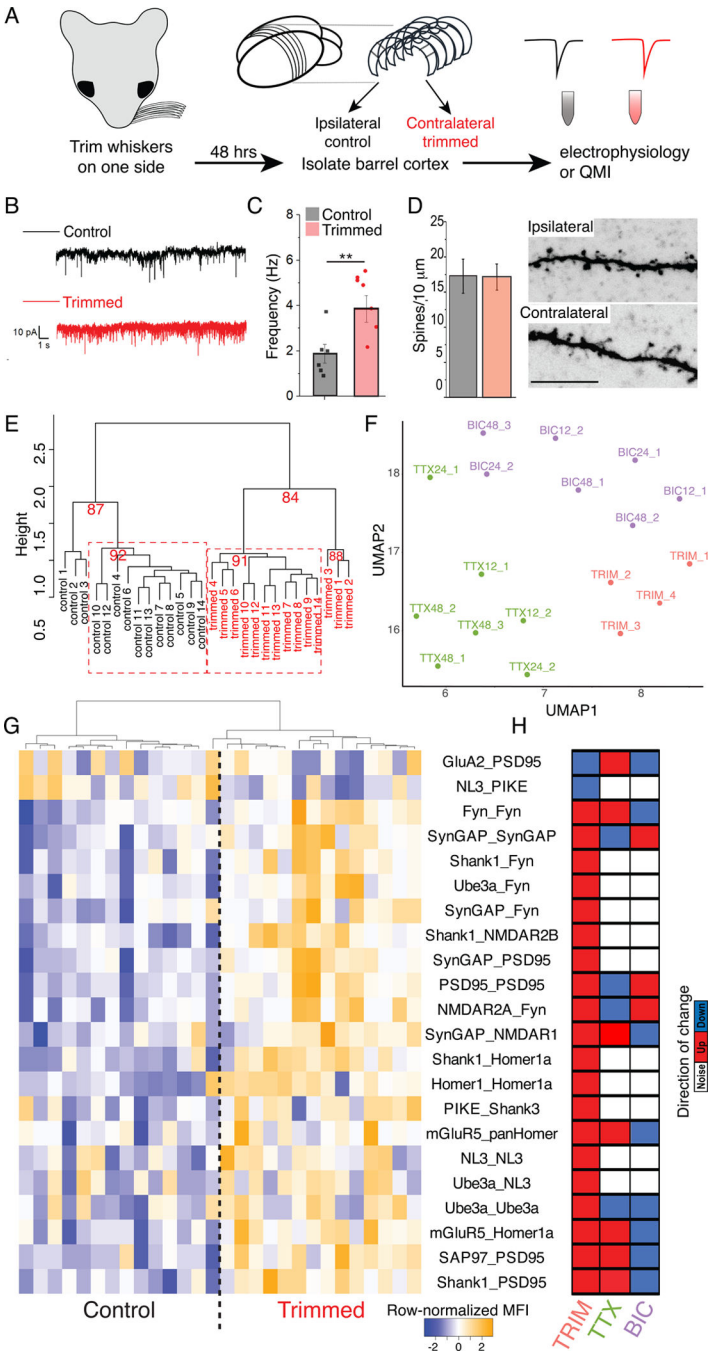

Fig. 2. Unilateral whisker trimming causes a homeostatic response in L2/3 pyramidal neurons of the contralateral barrel cortex.

(A) Experimental design illustrating 48 hours of unilateral whisker deprivation followed by either QMI or electrophysiology of the microdissected barrel cortex. **(B to D)** 20s raw traces (B), mean frequency of mEPSCs (C), and mean synaptic spine density (at 100–150 µm from the soma; D) from ipsilateral control (black) and contralateral trimmed (red) barrel cortex. Ipsilateral: N=6 (B, C) and 9 (D) cells; contralateral: N=7 (B, C) and 12 (D) cells. Scale bars: (B) 10pA, 1s; (D) 10 µm. ** $P<0.01$ by Student's t-Test. **(E)** Hierarchical clustering of

14 control and 14 trimmed hemispheres with AU *P*-values shown in red. **(F)** UMAP comparing in vitro upscaling, in vitro downscaling and in vivo whisker trimming. Each point represents a single set; N=4 biological replicates per set. **(G)** Heatmap of row-normalized MFI of ANC∩CNA PiSCES. Samples on the x-axis are arranged by unsupervised hierarchical clustering. N=14 biological replicates per condition. **(H)** Chart comparing the direction of change of ANC∩CNA PiSCES after whisker trim or in vitro upscaling or downscaling.

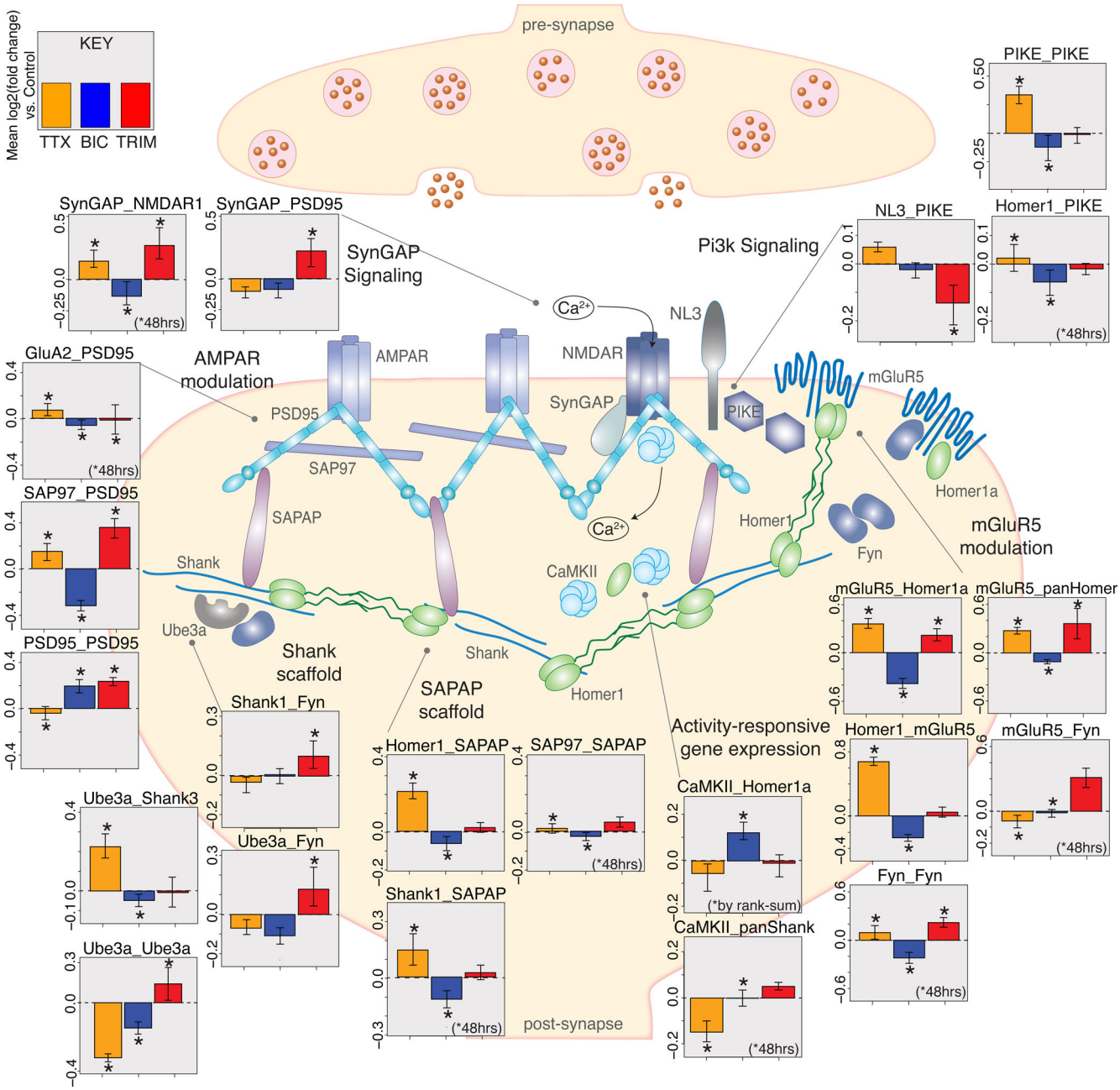

Fig. 3. Post-synaptic proteins that change during in vivo or in vitro homeostatic plasticity.

Simplified illustration of the excitatory synapse and select functional protein groups evaluated by QMI in the current study, positioned according to where interactions would occur. Bar graphs represent the mean $\log_2$(fold change) over control for the given PiSCES in all sets of experiments using the indicated perturbation ± SEM from N=6, 7, and 3 sets of 4 biological replicates for TTX, BIC, and whisker trimming, respectively. * P<0.05 by ANC∩CNA in the given condition.

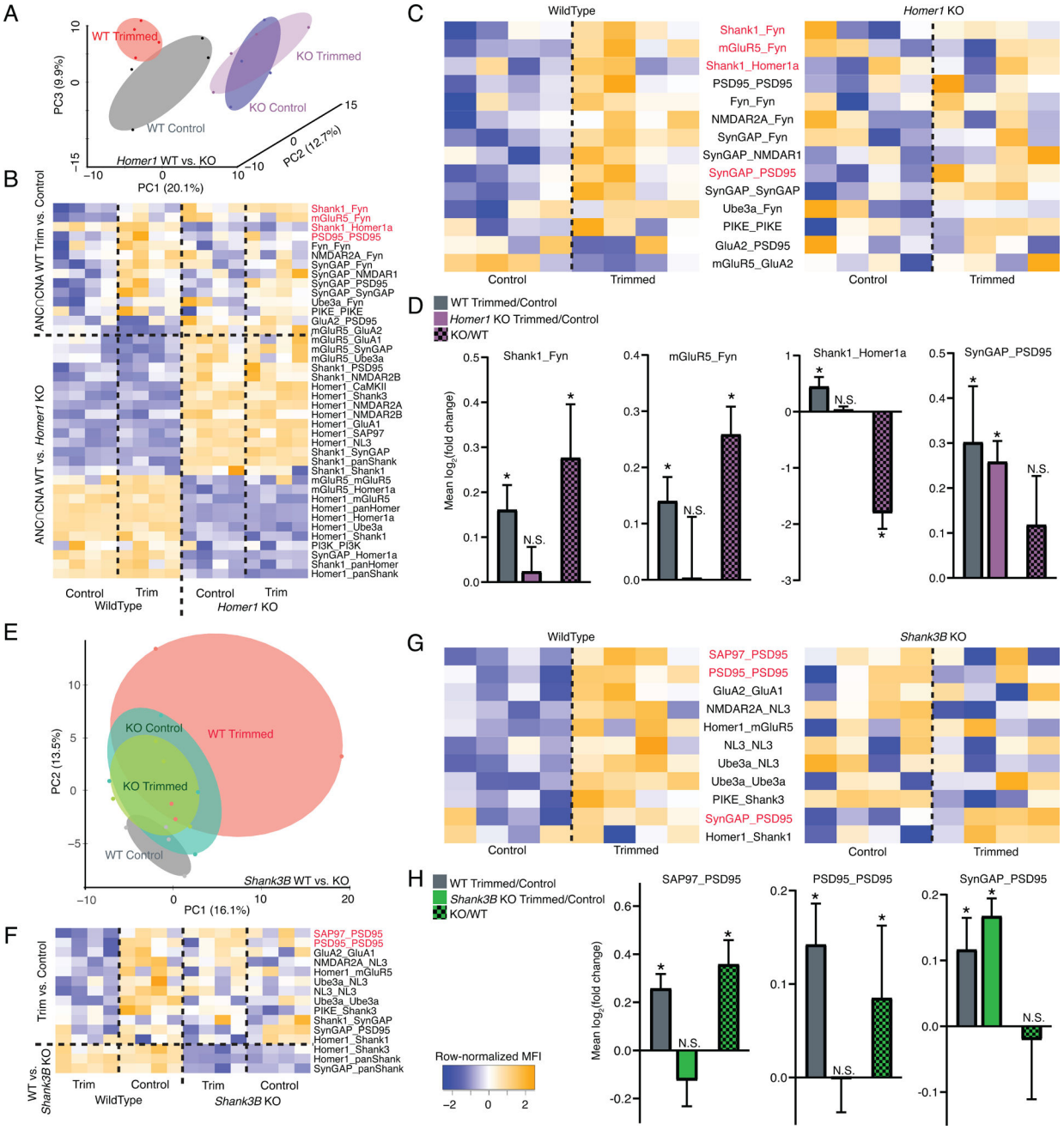

Fig. 4. Homeostatic plasticity is disrupted in the barrel cortex of mice mutant for *Homer1* and *Shank3*.

(A) PCA of sensory-deprived (trimmed) and control hemispheres of *Homer1* WT (red and black, respectively) and *Homer1* KO (purple and blue, respectively). **(B)** Heatmap of row-normalized MFI all PiSCES ANC∩CNA significant after whisker trimming or comparing WT and *Homer1* KO control hemispheres. **(C)** ANC∩CNA PiSCES that were significantly altered by whisker trimming ($P < 0.05$ by ANC), re-normalized to highlight genotype-dependent differences (WT, left panel; KO, right panel). **(D)** Bar graphs of mean $\log_2$(fold changes) of select PiSCES—those that are red in (B)—after whisker trimming in control and

Homer1 KO barrel cortex, and with baseline differences between WT and KO control hemispheres. * $P < 0.05$ by ANC. N=4 biological replicates per condition. **(E to H)** Assays and analyses as described in (A to D), in *Shank3B* WT and KO mice. N=4 biological replicates per condition.